García-Gómez, A.; Fernández-Blanco, AC.; Herance, JR.; Albero-Sancho, J.; García Gómez, H. (2017). Graphenes as additive in photoelectrocatalysis. Journal of Materials Chemistry. A: Materials for Energy and Sustainability. 5(32):16522-16536. doi:10.1039/C7TA04045H

Journal Name

ARTICLE

Graphenes as additive in photoelectrocatalysis

Alejandra García,[a] Cristina Fernández,[a] Jose R. Herance,[b] Josep Albero[a] and Hermenegildo García[a]

Received 00th January 20xx,
Accepted 00th January 20xx

DOI: 10.1039/x0xx00000x

www.rsc.org/

Due to their electrical conductivity, graphenes in small weight percentage can increase the efficiency of semiconducting catalysts. Besides conductivity, other reasons for this beneficial influence of graphenes in PEC are the large contact area with the particles of the semiconductor and the fast electron migration from the conduction band of the semiconductor to graphenes, enhancing charge separation efficiency and lifetime. The purpose of the present review is to show how addition of graphenes increases the photoelectrocatalytic activity of semiconductors as photoanodes or photocathodes. The existing literature has been grouped according to the photoelectrocatalytic reaction, including CO_2 reduction, H_2 generation and pollutant degradation, making emphasis in the photoelectrode preparation, since it determines the properties of the resulting composite. The final section summarizes the state of the art and forecasts future developments in the field.

Introduction

Due to the global warming and the need to decrease greenhouse gases emission to the atmosphere, the development of alternative green energy sources has become an urgent need. As inexhaustible green energy, solar light reaching the Earth surface is attracting considerable attention as one of the possible alternatives to the use of fossil fuels [1-3]. In this context, photocatalysis, aimed at converting photons into chemical energy, is one of the most explored techniques that could serve to obtain usable fuels from sunlight [4, 5].

In this regard, considerable research efforts are being carried out in order to prepare suitable photocatalysts for either solar-to-energy conversion as well as environmental remediation. [6-9] In particular, the search of photocatalysts capable exhibiting high performance in applications such as CO_2 reduction, water splitting, pollutant degradation and bacterial disinfection has attracted the interest of the scientific community in the last decade [10-13]. However, photocatalysis requires in many cases the use of sacrificial agents and exhibits low production rates, limiting severely its applicability. One possibility to circumvent the problem, increasing production rates and avoiding sacrificial agents, is to apply a bias potential to the photocatalyst that in this case should be in contact with an electrode [14]. Considering the increasing production of electricity by renewable energy, photoelectrocatalysis (PEC) is attracting an increasing attention because of its possibilities as method to convert solar energy into chemical energy with the required efficiency and productivity to reach commercialization [15]. The application of an electric field increases the separation of charge carriers in a semiconductor and may result in a light productivity rate of the target product. In this way, PEC combines the advantages of photocatalysis and electrocatalysis [16].

The focus of the present review is to describe the state of the art for the use of graphene in PEC. Considering the electrical conductivity of graphene and its growing use in photocatalysis as cocatalyst, there is much obvious potential on developing photoresponsive electrodes containing graphene for PEC.

Although there are a substantial number of articles in photocatalysis using graphene as co-catalyst in combination with semiconductors [17-19], they will not be considered in the present review that it is focused on the use of graphene and its derivatives in PEC. Also, those reports in where the photoresponse and the photocurrent of transparent conductive electrodes that have a thin layer of a semiconductor and graphene have been measured, without analyzing the products evolved in the photoelectrochemical process will not be necessarily included in this review.

Since Fujishima and Honda published the first observation of light-induced water electrolysis, using TiO_2 as photolectrode[20], a high number of semiconductors have been used for photocatalysis and PEC including ZnO, Fe_2O_3, WO_3, CdS, $BiVO_4$, Bi_2WO_4 and $NaTaO_3$[21]. However, it is clear that TiO_2 is still the most studied semiconductor owing to the combination of remarkable properties such as low cost, high photocatalytic activity under UV light irradiation and long term stability against corrosion[22, 23]. The main problem of TiO_2 is its wide energy band (3.2 eV) and as consequence, TiO_2 can only absorb UV light from solar energy, resulting in a very unsatisfactory TiO_2 photocatalytic activity under sunlight irradiation. To circumvent this limitation of TiO_2, several other

[a] *Instituto Universitario de Tecnología Química CSIC-UPV, Universitat Politècnica de València, Av. De los Naranjos s/n, 46022, Valencia, Spain.*
[b] *Grupo de Imagen Médica Molecular, Val d'Hebron Research Institut, CIBBIM-Nanomedicina, Pg. Vall d'Hebron 119-129, Barcelona, Spain.*

Electronic Supplementary Information (ESI) available: [details of any supplementary information available should be included here]. See DOI: 10.1039/x0xx00000x

semiconductor materials have been studied as visible light active photocatayst, such as metal sulfides or oxides, and metal nanoparticles[24-27]. General issues common to all photocatalysts are how to maximize solar energy absorption and decrease the electron-hole pair recombination.

Due to its unique properties, graphene has become a promising material in different fields ranging from renewable energy [28, 29] to catalysis [30-35]. The high electrical conductivity and charge mobility, its theoretical high specific surface area, the excellent optical transmittance and high chemical stability[36-38] allows graphenes to be used in different fields such as sensors [39-42], capacitors [43-45], transparent conductive films[46-49], nanocomposites, transistors [50-52] and catalysis [53]. Specifically in the field of solar-to-energy conversion, the use of different carbon based nanomaterials (graphene, graphene oxide, doped-graphenes, fullerenes, carbon nanotubes, carbon quantum dots…) either as photocatalysts [54-57] or as additive in semiconductors (LDHs, CdS, ZnS, TiO_2, ZnO, g-C_3N_4…) to improve their photocatalytic performance has grown very fast in the last years [58-61]. This enhanced photocatalytic efficiency derives from the occurrence of better charge separation due to the migration of photogenerated electrons in semiconductors to graphene and their consequent delocalization. A possible influence of graphene enlarging in the absorption range of the semiconductor has also been claimed [21, 62, 63]. The recent development of graphene-based photoelectrodes in solar-to-energy conversion is summarized in Figure 1. As can be observed, the number of publications per year has increased continuously in the last 5 years.

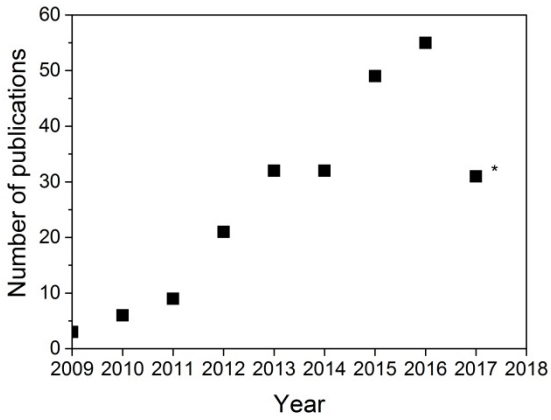

Figure 1. Number of publication related to the use of graphene-based materials as photoelectrodes in solar-to-energy conversion in the last years. * Number of publications up to June 1st of 2017. Source SciFinder ®

This review presents different materials composed by semiconductors and graphene as co-catalyst and electrical conductive material for their use in photoelectrochemistry in three main applications, i.e., in CO_2 reduction, H_2 production and pollutant degradation. When presenting the existing photoelectrodes, special attention will be paid to the preparation procedure, since it will determine the morphology of the composite and the resulting properties. Also the conditions of the photoelectrocatalytic cells will be commented particulary considering the potential role of the electrolyte not only to equilibrate charges, but also as sacrificial agent undergoing transformation during the photoelectrocalytic process. Stability of the graphene-containing photoelectrodes will also be commented when data on this issue has been provided.

Photoelectrochemical CO_2 reduction

There is a considerable number of studies showing that when semiconductor materials (TiO_2, WO_3, Cu_2O, ZnO, g-C_3N_4, etc.) are combined with graphene in very small weight percentages there is a synergetic effect [10, 64-67] and, as result, the photocatalytic activity is enhanced for H_2 generation [68-70] as well as for CO_2 reduction [71-75]. Not surprisingly in view of the effect of the addition of graphene in photocatalysis, some photoelectrochemical studies have also focused on establishing performance of TiO_2/graphene composite as photoanode[76, 77] in comparison with analogous photoelectrodes lacking graphene. In one of these studies TiO_2/graphene photoanode has been used to promote the photoelectrochemical CO_2 reduction in aqueous media[76]. TiO_2/graphene composite was prepared forming TiO_2 by sol-gel from tetra-n-buthyl orthotitanate [$Ti(OBu)_4$] in the presence of reduced graphene oxide (rGO). In this procedure a final calcination step at high temperature (600 °C) is required to induce the crystallization of the initially amorphous TiO_2 solid initially obtained by sol-gel into the anatase phase that is the photocatalytically most active TiO_2 crystallographic form. SEM characterization of TiO_2 samples containing or not rGO does not show differences in the average TiO_2 particles size (18-24 nm), but aggregation of these TiO_2 nanoparticles (NPs) is diminished by the presence of graphene, i. e. TiO_2 NPs exhibit less agglomeration and are more uniformly dispersed when graphene is present than in the absence of graphene. Differences in the UV-Vis absorption spectra show that the presence of rGO increases the absorption intensity compared with the sample lacking of rGO. It was commented that this higher absorption intensity should be beneficial for the photoelectrocatalytic process, since more photons could be absorbed. However, it should be pointed out that the higher absorptivity of TiO_2 when rGO is present is most probably due to an internal filter effect of few or multiple layer rGO sheets and, in this case, the photocatalytic activity should not be increased but decreased, since the photons are really not absorbed by TiO_2. While single layer graphene is almost completely transparent to all wavelengths in the UV-visible spectral range, transparency of the sample decreases and visually becomes grey or black in appearance is observed for few-layer graphene samples due to the occurrence of π-π stacking among the graphene layers.

Photoelectrochemical studies using the TiO_2/graphene photoanode indicate that the photocurrent in an aqueous solution containing Na_2SO_4 (0.1 M) and triethanolamine (TEA) (0.5 M) increases in the presence of CO_2, and this was taken as an indication that photocatalytic CO_2 reduction was taken

place, although product analysis is still necessary to confirm this assumption. The pH value influences the photocurrent in the presence of CO_2, reaching a maximum at pH 11. This was justified considering possible differences in photoelectrocatalytic reduction of HCO_3^- (7.5<pH<8.5) and CO_3^{2-} (dominant at pH>11.5), the latter one being less prone to undergo reduction. Accordingly, it seems that HCO_3^- is better substrate for the photoelectrochemical reduction and basic pH values are more favourable, provided that it does not change HCO_3^- speciation.

Electrochemical impedance spectroscopy (EIS) shows for TiO_2/graphene electrodes different arc sizes as a function of the pH. It was, then, concluded that the observation of higher photocurrent at higher pH values was due to the lower charge transfer resistance under these conditions. It was observed that the presence of graphene on the photoanode increases the anodic current of the TiO_2 electrode, a fact that was attributed to the conductive properties of graphene. However, it should be commented that the interest of this study would be higher if direct evidence of CO_2 reduction as well as the resulting product distribution would have been provided. This could have done by complete analysis of the aqueous as well as the gas phase during the photoelectrocatalytic study. Without this data, the proposed synergy of graphene on the photoelectrocatalytic HCO_3^- reduction cannot be considered as confirmed on solid ground.

The interaction of CO_2 with TiO_2 nanoparticles supported on G or r-GO (containing preferentially epoxy groups) has been studied in models using density functional theory (DFT) calculations. This work revealed that the type of G supporting TiO_2 should exert a significant influence on the CO_2 binding energy. Thus, it is predicted that r-GO containing mainly epoxy groups should adsorb stronger CO_2 on the TiO_2 surface, due to a higher charge delocalization on the r-GO sheet when compared with TiO_2 supported in G [78].

Photoelectrocatalytic CO_2 reduction has been reported also by Hasan and co-workers using Cu-doped TiO_2 supported on rGO ((Cu)TiO_2-rGO)[77]. Cu doping (at nominal 1 mol%) and formation of the composite of doped TiO_2 and graphene was achieved by synthesizing TiO_2 (30-45 nm) by sol-gel from $Ti(OBu)_4$ in an ethanol/water solution in the presence of $Cu(NO_3)_2$ as dopant precursor and 1 wt% rGO. The preparation procedure was completed by calcination of the material at 450 °C for 4 h. The anatase phase of TiO_2 in this composite was confirmed by XRD, while Cu phases were not detectable, something not surprising considering the low Cu proportion in the material. The presence of Cu as Cu^{2+} and Cu^+ (56 %) could be, however, detected and differentiated by XPS. The strongest evidence in support of Cu doping into the TiO_2 framework was obtained by HR-TEM measurements. *d*-Spacing of Cu-doped TiO_2 was 0.35 and 0.26 nm for two different facets. The presence of Cu atoms in the lattice caused an enhancement of light absorption of the doped TiO_2 sample in the 400-800 nm range. A decrease in the emission intensity of (Cu)TiO_2-rGO was observed in photoluminescence, suggesting a decrease in the efficiency of e^-/h^+ recombination that is the process responsible for light emission. In addition, EIS also shows lower resistance of the semiconductor/electrolyte interface for (Cu)TiO_2-rGO compared to related binary materials. Moreover (Cu)TiO_2-rGO electrodes resistance decreases from 536.9 to 217 $\Omega \cdot cm^{-1}$ for dark and illuminated electrodes, respectively, due to the generation of photocurrent.

With regard to the photoelectrocatalytic CO_2 reduction, irradiation of (Cu)TiO_2-rGO in 10 % aqueous solutions of methyl diethanolamine (MDEA) saturated with CO_2 gives rise to formation of methanol and formic acid (quantified by HPLC). No photocurrent was observed for TiO_2 and TiO_2-rGO, while (Cu)TiO_2-rGO exhibits a maximum photocurrent at a bias potential of -0.61 V *vs* SCE. The estimated electrical current-to-chemical reduction efficiency was 32.47 % that is a remarkable value and probably enough for commercial application provided that the process can be performed under natural sunlight irradiation in the absence of sacrificial MDEA and the photoelectrode is stable for very long periods.

The photoelectrochemical CO_2 reduction has also been reported by Hasan and co-workers for Ga_2O_3-TiO_2-rGO composite deposited on ITO electrode[79]. The reason for combining Ga and Ti oxides is to determine the effect of $3d^{10}$ Ga cations in one phase with $3d^0$ Ti atoms in another phase. The preparation of the composite was carried out by sol-gel hydrolysis starting from $Ti(OBu)_4$ and $Ga(NO_3)_3$ under acid conditions (acetic acid pH<3) in the presence of suspended rGO. rGO was obtained by hydrazine reduction of GO prepared by Hummers oxidation of graphite. The photoanode was finally prepared by electrophoretic deposition of the suspension containing the three components. No analytical data of the final composition of the photoanode was given, although 1 mol% $Ga(NO_3)_3$ is used in the synthesis and the rGO content in the suspension was 1 wt%. Ga_2O_3-TiO_2-rGO composite was calcined at 550 °C in order to crystalize the anatase phase. Although Ga doping of TiO_2 was claimed in accordance with its small percentage, X-ray diffraction clearly revealed two peaks at 37.6 and 38.5° corresponding to β-Ga_2O_3 indicating that, at least in part, Ga is present in a separate phase.

The photoelectrochemical activity Ga_2O_3-TiO_2-rGO for CO_2 reduction in the presence of triethylamine (TEA) was evidenced by the remarkable increase in the voltammetry response when the photoanode containing this nanocomposite was illuminated after CO_2 saturation, while in the absence of CO_2 the photocurrent is negligible (see Figure 2) and formic acid is not detectable. This remarkable increase in the current density was taken as an evidence of the occurrence of CO_2 reduction.

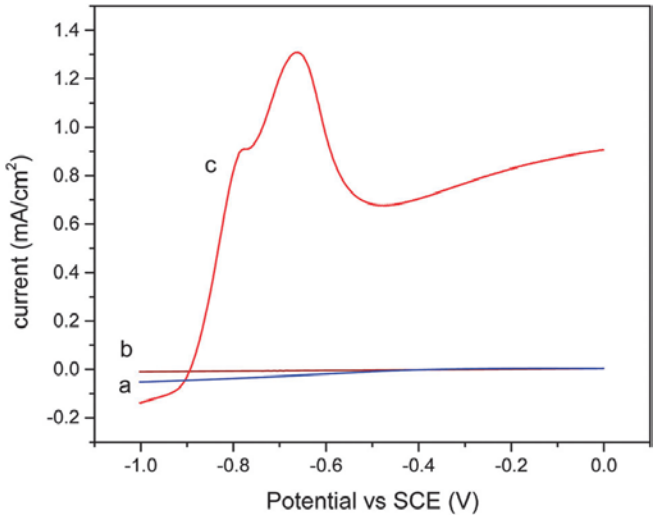

Figure 2. Voltammetric response of the illuminated Ga_2O_3–TiO_2-rGO/ITO electrode in the presence of 5% TEA solution (a) in the dark, (b) under illumination with a solar simulator and (c) under illumination with CO_2 saturated solution. Reproduced from ref. [79] with permission from The Royal Society of Chemistry.

However, it should be commented that performing the photoelectrochemical reduction at -0.57 V *vs* SCE constant potential, the concentration of formic acid, although increasing linearly with the time, is very small, reaching 178 ppm at 2 h. The study should have been completed by i) quantifying the selectivity of the CO_2 reduction process *versus* hydrogen evolution, ii) by given efficiencies of CO_2 reduction, and iii) by providing data of a control at same conditions in the absence of rGO and/or Ga in the photoanode.

Cheng and co-workers developed a photoelectrocatalytic cell for CO_2 reduction by water consisting in a photoanode made of TiO_2 nanotubes and Pt NPs supported on rGO and deposited on a conductive Cu foam separated by a Nafion membrane[80]. Note that in this system rGO is not in contact with the semiconductor, but it is acting as support of Pt NPs. The scheme of the cell is similar to that shown in Figure 3. Also worth noting is that in these experiments different electrolytes for the photoanode (0.5 M H_2SO_4) and cathode (0.5 M $NaHCO_3$) compartments were used. The proton conductivity of Nafion membrane and the photoelectrocatalytic reaction should at long term equilibrate these two electrolytes, resulting presumably in a much decrease activity of the system.

The Pt NPs-rGO (with a particle size of 3.6 nm and a loading of Pt between 1 and 16 wt%) cathode was prepared by ethylene glycol reduction of $H_2PtCl_6{\cdot}6H_2O$ in the presence of dispersed GO obtained by Hummers oxidation of graphite. Pt-rGO powders were suspended in a mixture of Nafion solution and deionized water (1:1) and deposited on Cu foam, although no indication of the adherence of the Pt-rGO on Cu foam was given.

A synergistic effect of the photoelectrocatalytic process combining light and electrode polarization was observed by comparing the performance of the CO_2 reduction (2 V bias voltage and light) of the photoelectrocatalytic reaction with respect two control experiments, one of the purely photocatalytic (light, but not voltage) and other solely

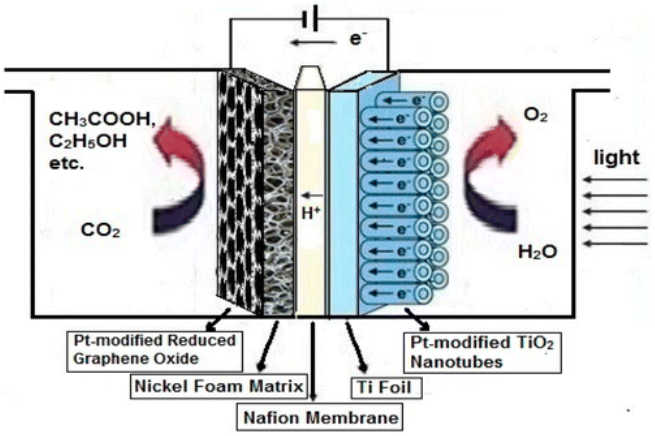

Figure 3. Schematic diagram of the photoelectrocatalytic system comprising TiO_2 nanotubes as photoanode and Pt-rGO supported on a metal foam as catode. The metal combines Cu or Ni. Reprinted with permission from ref. [81] Copyright (2014) American Chemical Society.

electrocatalytic (2 V bias potential, no light) reaction. Figure 4 summarizes the products obtained and illustrates the advantage of combining light and polarization potential.

One important finding of the photoelectrocatalytic CO_2 reduction process using Pt-rGO/Cu foam was also the synergy between Pt-rGO and the Cu foam, since both components independently are active for CO_2 reduction to C_1 and C_2 carboxylic acids and in the case of Pt-rGO also to methanol and ethanol. When the two components (Pt-rGO and Cu) are combined forming the cathode, propionic acid is also detectable in a significant extent and the overall rate of CO_2 reduction increases from about 1500 nmol·h^{-1}·cm^{-2} to about 2850 nmol·h^{-1}·cm^{-2}. It would be important to determine the origin of this synergy in order to maximize the effect. By studying the performance of a series of Pt-rGO samples with various Pt loadings, an optimal Pt loading on rGO of 4 wt% was determined to maximize CO_2 reduction, reaching a conversion rate of about 4000 nmol·h^{-1}·cm^{-2}.

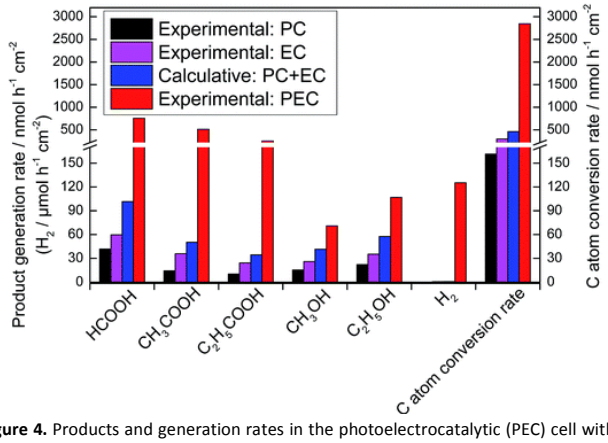

Figure 4. Products and generation rates in the photoelectrocatalytic (PEC) cell with Pt–rGO/Cu foam cathode and TiO_2 nanotube photoanode. Note: (1) PEC: voltage applied through the cell was 2 V. The Pt–rGO loading amount on Cu foam was 4 mg·cm^{-2}. Pt loading amount on rGO was 2 wt%. (2) Photocatalytic (PC): no voltage was applied through the cell. The connection between cathode and anode was through an external wire. (3) Electrocatalytic (EC): TiO_2 nanotubes in the dark. Reprinted with permission from ref. [80]. Copyright (2015) American Chemical Society.

The existence of an optimal Pt loading is related to the agglomeration of Pt NPs on rGO resulting in larger metal particles with lower activity when Pt NP loading is too high. As can be observed the products generated during the CO_2 reduction with Pt-rGO (formic, acetic, propionic acid, methanol and ethanol) have a particularly high economic value since they are liquids and many of them have two or three carbon atom chains.

When instead of Cu, a Ni foam is used as support, lower photoelectrocatalytic CO_2 reduction rate by water was measured (approximately 1130 nmol·h^{-1}·cm^{-2}), even if the TiO_2 nanotube array is modified with Pt NPs by electrodeposition to favour the e^-/h^+ separation and the electrical conductivity of the anode[81]. However, it should be commented that in the measurements with Ni foam cell, H_2SO_4 in the photoanode compartment present in the study with Cu foam was replaced by 1 M NaCl as electrolyte (Figure 4).

The origin of the photoproducts was confirmed to be CO_2 by performing a control experiment replacing 1 M $NaHCO_3$ electrolyte by 1 M Na_2SO_4, whereby only H_2 evolution was detected. ^{13}C-isotope labelling of CO_2 could have also confirmed the origin of the photoproducts on a firm ground. Comparing the performance of a cell having Pt-rGO deposited on Ni with analogous cathode containing Pt-CNT (CNT: carbon nanotubes) and Pt-C (C: active carbon) it was concluded that rGO is the most active material. Moreover, product selectivity for the CO_2 reduction changes from methane, formic and acetic acid when Pt-CNT is used to ethanol (major) and acetic acid (minor) using Pt-rGO. The current efficiency reached with the Pt-rGO cathode is 78 % in total. This is a very interesting product distribution due to formation at some stage in the reaction mechanism of C-C bonds, increasing considerably the added value of the products that could be used not only as solar fuels, but also as primary products for the chemical industry. The higher efficiency of Pt supported on rGO compared to other related carbon materials should be related to the unique morphological and physical properties of rGO, including electrical conductivity, single-atom layer thickness and large surface area.

In a pioneer work, Grimes and co-workers showed that N-doped TiO_2 nanotubes containing Pt and Cu NPs exhibit high activity for the natural sunlight, photocatalytic gas-phase CO_2 reduction by water to methane[82]. The system reached an efficiency of 111 ppm·cm^{-2}·h^{-1} that is among the highest rate reported for this reaction. The high activity for this catalytic system derived from a combination of factors including N-doping of TiO_2 to promote visible light absorption by narrowing TiO_2 band gap due to the presence N-atoms and/or oxygen vacancies and the presence of Pt and Cu NPs as co-catalysts to increase selectivity for CO_2 reduction and methane formation respect to alternative H_2 generation[82].

In this context, it is of interest to test this multicomponent material also under photoelectrochemical conditions. Bias voltage could increase even further the efficiency of the N-doped TiO_2 nanotube array for CO_2 reduction. Working in this field, Cheng and co-workers reported the photoelectrochemical reduction of HCO_3^- electrolyte in CO_2-saturated H_2O using a Pt-modified TiO_2 nanotube array grown on Ti foil that was used as photoanode, combined with Pt modified rGO as cathode[83]. Figure 5 illustrates the configuration of the two-compartment photoelectrochemical cell employed in these experiments. The operation potential range was scanned from +1.4 V to +2.6 V, finding that product generation increases steadily with the applied voltage, but the current efficiency has an optimal about 2 V. The analysed products included hydrogen, methane, carbon monoxide, formic acid, methanol, acetic acid and ethanol. A maximum carbon conversion rate of 1500 nmol·h^{-1}·cm^{-1} was reached at a bias voltage of 2 V upon irradiation from 320 nm to 410 nm. From the application point of view, it would be necessary to increase the selectivity of the process.

The influence of the applied bias voltage on the carbon atom conversion rate in the range potential from 1.4 V to 2.6 V shows that the amount of products formed, in particular acetic acid and ethanol, increases with the voltage as indicated the Figure 6. However, it should be commented that the current efficiency for CO_2 reduction first grows and, then, decreases when the bias voltage of the cell exceeds 2 V, due to the competitive H_2O electrolysis, whose efficiency increases above 2 V.

Concerning the optimal pH value of the cathodic electrolyte (1 M $NaHCO_3$) for achieving the highest product generation rate in CO_2 reduction, it was found that the maximum product formation was reached at pH 8.8, decreasing this rate for lower or higher pH values. This pH dependency is likely to be related with speciation of HCO_3^- in the aqueous phase.

Besides metal oxides, metal sulfides have also been widely used as semiconductors. The main advantage is that the band gap of sulfides (typically below 2.5 eV) is generally much narrower than oxides[84, 85]. Consequently, metal sulfides absorb in the visible wavelength range. One of the studies using metal sulfides as semiconductor reports the activity of a mixed copper-indium sulfide as photocathode for the CO_2 reduction

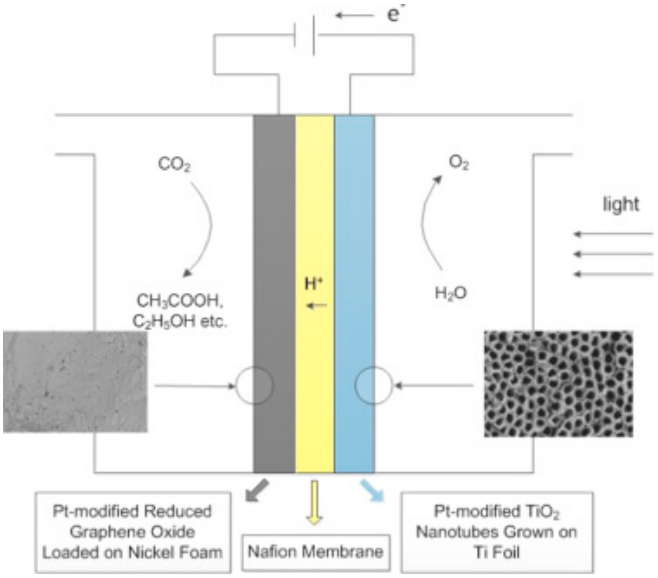

Figure 5. Schematic of the photoelectrochemical cell used for CO_2 conversion with N-doped TiO_2 nanotube arrays as photoanode and Pt-rGO as cathode. Reprinted with permission from ref. [83]. Copyright (2014) Elseview.

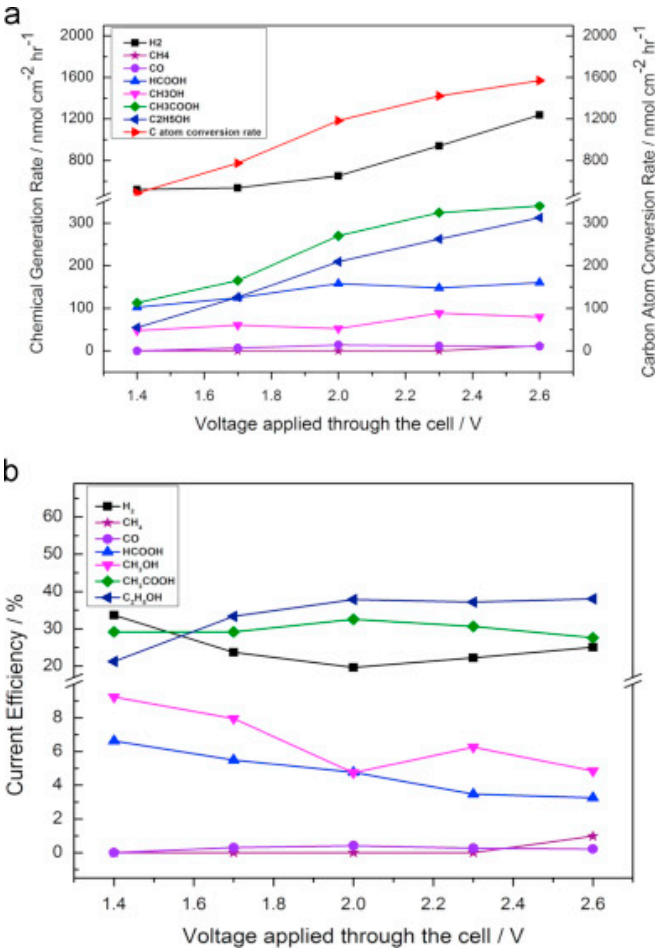

Figure 6. Carbon atom conversion rate (a) and current efficiency (b) in a photoelectrochemical cell with Pt-TiO_2 nanotubes photoanode and Pt-modified rGO (Pt-rGO) cathode under various applied voltages:. Note: Pt-rGO reduced for 24 h was used as cathode catalyst, and 110 pore per inch nickel foam was used as catalyst support. Reprinted with permission from ref. [83]. Copyright (2014) Elseview.

in absence and in presence of rGO as co-catalyst[86]. $CuInS_2$ cathode containing or not rGO was prepared by electrodeposition on a conductive transparent indium tin oxide (ITO) electrode from a dimethyl sulfoxide (DMSO) solution that contained an equimolar concentration of $CuCl_2$ and $InCl_3{\cdot}4H_2O$ and three times excess or sulfur powder. For the preparation of $CuInS_2$/rGO photocathode, GO in different concentrations was present during the electrodeposition of $CuInS_2$ to form $CuInS_2$/rGO. It is supposed that the GO undergoes simultaneous electrochemical reduction during the electrochemical deposition of $CuInS_2$/rGO. The better performance of the photocathode containing rGO was determined by comparing the current density *versus* bias voltage for $CuInS_2$ and $CuInS_2$/rGO electrodes in the dark and under UV-Vis illumination (350-650 nm). Figure 7 shows the photocurrent for this photocathode, showing the beneficial effect of the presence of rGO in the photocurrent generated by the photocathode. By applying an optimal bias voltage of -0.59 V and using as electrolyte 0.1 M acetate buffer solution and 10 mM pyridine under CO_2 saturation (pH value 5.2), methanol was the only product detected with an efficiency of

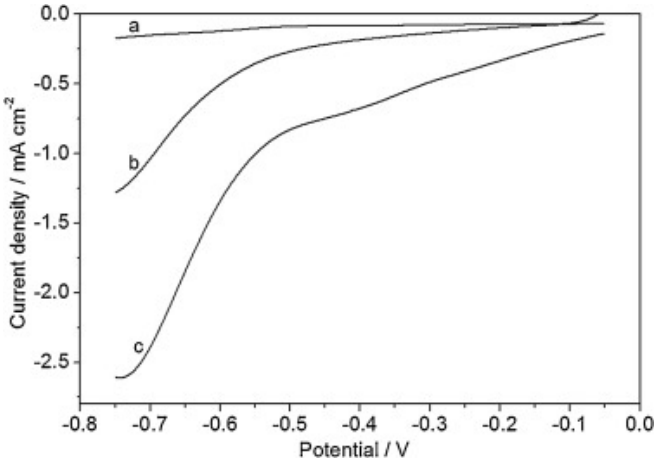

Figure 7. Photocurrent density for $CuInS_2$ and $CuInS_2$/rGO hybrid thin films in the potential range from -0.8 to 0 V in 0.1 M Na_2SO_4 aqueous solution (a) in dark, (b) $CuInS_2$ thin film under illumination, and (c) $CuInS_2$/rGO hybrid thin film under illumination. Reprinted with permission from ref.[86]. Copyright (2016) ScienceDirect.

1.4 % for $CuInS_2$/rGO photocathode that was higher than for $CuInS_2$ in the absence of rGO. Control experiments indicate that no methanol was formed in the absence of pyridine or in the presence of pyridine without acetate buffer. The reasons for this requirement of the simultaneous presence of acetate buffer and pyridine in the CO_2 reduction are not clear, because the obvious presumable role of both components should be pH control. In fact, the effect of the pH value on the current density and methanol concentration is remarkable, finding that 5.2 units is the optimal value. It was proposed that at this pH of 5.2, equimolar concentrations of pyridine and pyridinium should exist and the simultaneous presence of both species is optimal for the formation of $C_5H_5N\text{-}H^{+}\cdots O{=}C{=}O$ intermediate that is proposed to be the key species in the CO_2 reduction to methanol.

One of the main problems when metal sulfides are used as photocatalysts is the poor stability under operation conditions and their tendency to undergo photocorrosion, leading to the formation of the corresponding metal oxides. However, in the present case the linearity of methanol concentration with the irradiation time (in the mM range, see Figure 8) as well as the absence of change in the morphology of $CuInS_2$ and $CuInS_2$/rGO electrodes during the reaction suggest the stability of the mixed sulfide under the reaction conditions. Nevertheless, it should be commented that 10 h of reaction time could not be long enough to observe changes due to corrosion that could appear at longer times.

Table 1 summarizes the graphene-based photoelectrodes reported in this section as well as their working conditions and performance.

Table1. Summary of graphene-based photoelectrodes for reported for CO_2 reduction with indication of the applied bias potential, products formed and their performance.

Sample	Bias(V)	Products	Performance	Ref.
TiO_2/rGO	-	No analysis	-	74
(Cu)TiO_2/rGO	-0.61	CH_3OH and HCOOH	32.5%[a]	75
Ga_2O_3-TiO_2-rGO	-0.57	HCCOH	178 ppm[b]	77
Pt /Cu/rGO	2	HCOOH, CH_3COOH, C_2H_5OH, CH_3OH, C_2H_5COOH, H_2	[c] 4000 nmol/h·cm^2	78
Pt NPs-rGO	2	CH_4, CO, H_2, HCOOH, CH_3OH, CH_3COOH, C_2H_5OH	[d] 1500 nmol/h·cm^2	81
$CuInS_2$/rGO	0.59	CH_3OH	1.4 %	84

[a] referred to current-to-chemical reduction efficiency. [b] total HCOOH production in 2h. [c] Maximum CO_2 conversion rate. [d] Maximum CO_2 conversion rate.

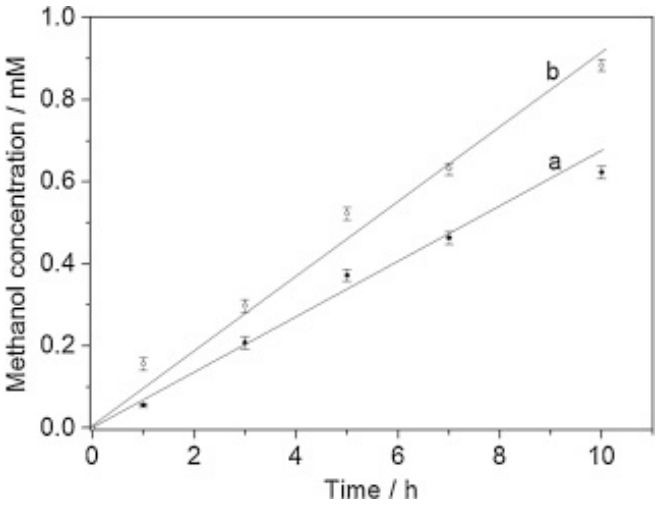

Figure 8. Temporal evolution of methanol using (a) $CuInS_2$ and (b) $CuInS_2$/rGO hybrid thin film electrodes at −0.59 V. Reprinted with permission from ref.[86]. Copyright (2016) ScienceDirect.

Photoelectrochemical hydrogen production

Besides CO_2 reduction, the use of solar light to obtain H_2 from H_2O in the presence of a photocatalyst has been widely studied as a possibility for the renewable, clean and large-scale production fuel [87-89]. However, the strict thermodynamic requirements, on one hand, and the need to use of narrow band gap semiconductor materials to harvest the maximum possible visible light photons, on the other hand, explain why the current state of the art has achieved insufficient efficiencies (~1%) for large scale industrialization [90]. And for this reason, PEC is being considered, among other methodologies, a very promising approach for the generation of H_2 from H_2O [91].

Although TiO_2 is by far the most widely used photocatalyst combined with rGO for photoelectrochemical hydrogen generation,[92, 93] other semiconductors have also been combined with rGO for their used as photoelectrodes.

In one of these studies, Ng and co-workers used $BiVO_4$ as photocatalyst to promote visible light (λ > 420 nm) reduction of GO to rGO in ethanol suspension and then $BiVO_4$-rGO was drop-cast on and ITO electrode. In comparison to $BiVO_4$, the composite $BiVO_4$-rGO exhibits significantly higher photoresponse in the voltage range from -0.5 V to +1 V [94]. Figure 9 shows the incident photon to current efficiency (IPCE) values at +0.75 V bias of $BiVO_4$-rGO photoelectrocatalyst that is considerably higher than analogous $BiVO_4$ electrode.

The efficient photorresponse presented in Figure 9 is also reflected in the much higher efficiency of $BiVO_4$-rGO composite for water splitting into H_2 and O_2 using 0.1 M of Na_2SO_4 electrolyte at an external bias of 0.8 V, reaching an evolution rate of 0.75 and 0.21 μmol·h^{-1} for H_2 and O_2, respectively. This higher efficiency of $BiVO_4$-rGO is attributed to the slower charge recombination due to the presence of rGO that promotes charge separation and facilitates the electron transport from $BiVO_4$ to ITO electrode. Other role for the rGO sheets is to provide a good dispersion of $BiVO_4$ particles and improve the contact of these particles with the surface of rGO.

In a different approach, Ke et al. developed a three component photoelectrode composed by TiO_2 beads/Ag/G for the photoelectrochemical hydrogen production [95]. They found that incorporation of the G sheets on the TiO_2 based photoanode improved the charge collection efficiency. On the other hand, light harvesting enhancement was achieved through either light scattering of TiO_2 beads or by excitation of the resonance surface plasmon of the Ag nanoparticles.[95]

In another three component nanostructured photoelectrode the combination of TiO_2 nanowires with rGO and Cu_2O was evaluated as photoanode for hydrogen production under UV-Vis light irradiation in the presence of methanol as sacrificial

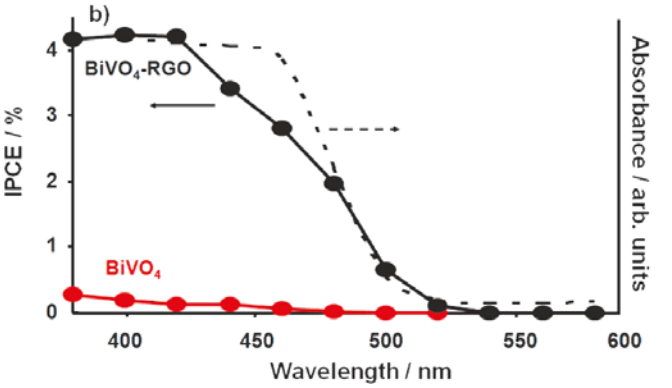

Figure 9. IPCE and diffuse reflectance spectra of $BiVO_4$ and $BiVO_4$-rGO. Reprinted with permission from ref. [94]. Copyright (2010) American Chemical Society.

electron donor at 0.6 V bias potential[96]. The rationale behind the preparation of this photoanode was to increase the interfacial contact between TiO_2 and Cu_2O that was considered as one of the main reasons for the limited efficiency of the Cu_2O/TiO_2 heterojunction. The photoelectrode was prepared by synthesizing TiO_2 nanowires on fluorine doped tin oxide (FTO) by hydrothermal deposition using $Ti(OBu)_4$ as precursor and HCl to promote its hydrolysis and condensation at 180 °C for 6 h, followed by calcination at 450 °C for 2 h to increase the

crystallinity of the nanowires. FE-SEM images show that these nanowires grow perpendicular to FTO. Subsequently, GO suspended in water was deposited on the thermal-treated TiO_2 nanowires and then reduced *in-situ* by heating under N_2 at 400 °C and final UV light irradiation. Then, Cu_2O was deposited starting from Cu^{2+} solution that was reduced on the electrode by Na_2SO_3. Figure 10 summarizes the process for the preparation of FTO/TiO_2/rGO/Cu_2O.

The photoelectrode was characterized by XRD, Raman and XP spectroscopy. These techniques are in agreement with the formation of each of the three components. The nanowire morphology of TiO_2 (170 nm average), the presence of rGO nanosheet and the process of deposition of Cu_2O was followed by FE-SEM. As it was expected, while TiO_2 nanowires absorb from 200 to 400 nm and rGO has not influence in the absorption spectrum, deposition of increasing amounts of Cu_2O shifts the onset of the absorption spectrum from 400 beyond 550 nm.

Importantly, FTO/TiO_2/rGO/Cu_2O photoelectrode exhibits a high photocurrent reaching more than 0.1 mA·cm^{-2} at 0.8 V upon illumination with a Xe lamp (UV-Vis) with an optimal amount of TiO_2 deposited on the electrode. This better performance of FTO/TiO_2/rGO/Cu_2O is in agreement with the expected role of each of the components promoting electron transfer as well as the observed visible light photoresponse due to the presence of Cu_2O.

FTO/TiO_2/rGO/Cu_2O exhibits the lower resistance for charge transfer in the series of control samples tested. The IPCE values at 0.6 V *versus* Ag/AgCl of bias voltage for the

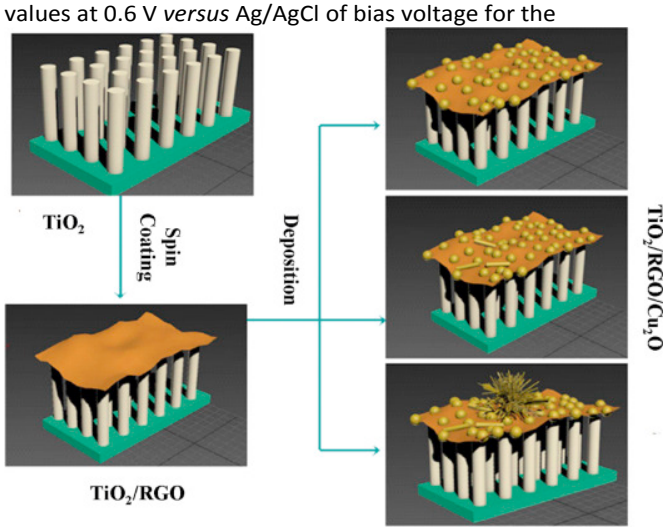

Figure 10. Schematic illustration of the synthesis of FTO/TiO_2/rGO/Cu_2O heterostructured photoelectrodes. Reprinted with permission from ref. [96]. Copyright (2016) ScienceDirect.

multicomponent FTO/TiO_2/rGO/Cu_2O photoelectrode reaches a value of 55 % in the 370 – 400 nm region, appearing an obvious peak in the visible region from 425 – 450 nm that was attributed to the photoresponse derived from Cu_2O.

The performance of the FTO/TiO_2/rGO/Cu_2O as photoanode for hydrogen production and methanol oxidation (20 % aqueous solution) was tested in a two compartment cell sketched in Figure 11.

At 0.6 V *vs* SCE electrode bias potential under Xe lamp irradiation the hydrogen production rates for TiO_2 and FTO/TiO_2/rGO/Cu_2O were in average rate of 211.8 and 631.6 μmol·h^{-1}·m^{-2}, respectively. It is proposed that the presence of rGO and Cu_2O decreases the electron-hole recombination and enhances the electron transport to the transparent conductive electrode. The long term stability of the FTO/TiO_2/rGO/Cu_2O photoelectrode was determined for 10 h, observing that the current density even increases during this time. This stability was attributed to the positive effect of methanol as reducing agent that maintains Cu atoms as Cu(I) ions during the operation of the system, the increase in the current density being attributed to a favorable change in the morphology of these particles.

It is worthy noticing that introduction of doped-G in contact with semiconductors can promote the formation of p-n heterojunctions which could enhance photoelectrochemical H_2 production due to favorable charge transfer between the p- and n-type semiconductor materials.

In this regard, Hong and Nam reported the deposition of G monolayers on top of Si photocathodes and subsequent plasma treatment in N_2 atmosphere in order to induce the incorporation of abundant nitrogen atoms in the G net [97]. This nitrogen doped G exhibited a remarkable increase in the exchange current density as well as a significant anodic shift of the photocurrent onset. Moreover, the N-doped G acts as passivating agent, inhibiting Si surface oxidation during operation of the photoelectrode in water solutions, enhancing the chemical stability of the Si photocathode [97].

In similar approach, S. Agnoli and co-workers reported a one-pot synthesis of N-doped G / MoS_2 nanocomposite which was seven times more efficient that single MoS_2 electrodes [98]. They claimed that the nitrogen dopant in G provided anchoring sites to MoS_2, providing local p-n heterojunctions which allowed more efficient charge separation [98]. Moreover, theoretical calculations in MoS_2 has revealed that, in spite of its very promising ability for H_2 production, derived from the edges of its 2D layers [99], the main drawbacks of this material for implementation in commercial applications are derived from its limited surface area, the few exposed active edge, and its low conductivity [100]. These limitations have been overcome through deposition of MoS_2 on G surface. In fact, Zhu et al. carry out a theoretical and experimental work in order to explain this behavior [101]. They found that there is a direct relationship between electrode conductivity and the H_2 production performance. Thus, based on first-principles calculations, they establish how an excess of negative charge density in the electrode affects the variation of Gibbs free energy and therefore, the H_2 production performance [101].

Continuing with the photoelectrocatalytic performance of the combination of metal sulfide and graphene, Zhang and co-workers reported the preparation of $Cd_XZn_{1-X}S$ sheets with lateral dimensions in the micrometre range, containing diethylenetriamine (DETA) and having nanopores as it can be observed in Figure 12 [102]. This material was obtained starting from ZnS-DETA that was submitted to ion-exchange with Cd^{2+} at 160 °C for 6 h. This hydrothermal treatment replaced in the

inorganic-organic hybrid sheet part of Zn^{2+} ions by Cd^{2+} and at the same time created some porosity on the sheet around 5 nm of diameter.

Upon visible light irradiation in water containing Na_2S and Na_2SO_3 as sacrificial electron donor this material generates hydrogen at a rate of 1.67 $mmol \cdot g^{-1} \cdot h^{-1}$. In a further development of the same material, these authors prepared a

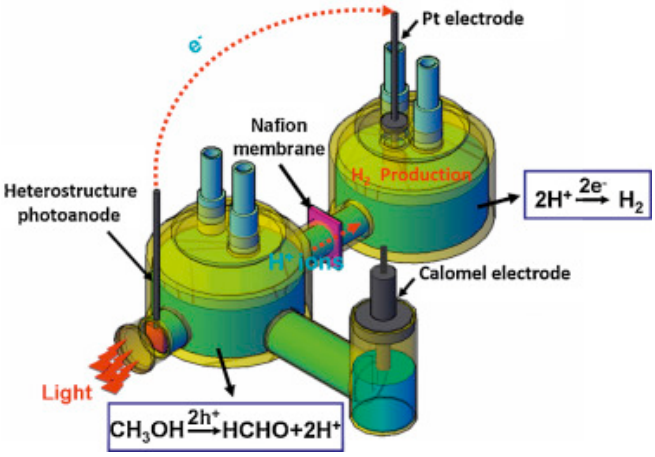

Figure 11. Schematic diagram of the two-compartment cell used equipment for photoelectrochemical hydrogen production by methanol decomposition. Schematic illustration of the synthesis of FTO/TiO2/rGO/Cu2O heterostructured photoelectrodes. Reprinted with permission from ref. [96]. Copyright (2016) ScienceDirect.

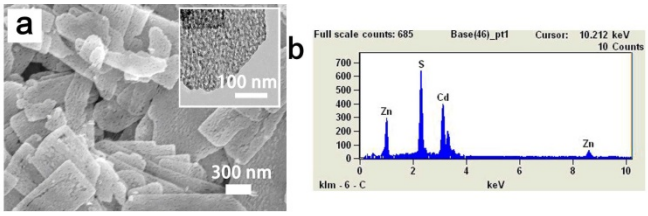

Figure 12. (a) SEM and TEM (inset) images and (b) EDX spectrum of nanoporous $Zn_{0.5}Cd_{0.5}S$ nanosheets. Reprinted with permission from ref.[103]. Copyright (2014) ScienceDirect.

composite of $Zn_{0.5}Cd_{0.5}S$ and 5 % of rGO and used the composite for the photoelectrocatalytic visible light generation of hydrogen[103]. A three-electrode cell, photoanode, Pt foil as counter electrode and saturated calomel (SCE) as reference electrode, and at a bias potential of 0.6 V generates hydrogen at a rate of 12.05 $\mu mol \cdot h^{-1} cm^{-2}$. Figure 13 shows the temporal evolution of H_2 for two different potentials.

The photoelectrode containing rGO enjoyed a high stability with a steady hydrogen generation for 3 h. However, it should be commented that besides as sacrificial electron donor, the presence of S^{2-} in the solution should increase the stability of the chalcogenide and in the absence of S^{2-} photocorrosion of the mixed metal sulfide could probably occur.

It has been observed that in this system, the presence of rGO in the composite influences the photocurrent density that increases gradually along the rGO content in the range from 1 to 5 %, decreasing somewhat the H_2 production rate when the amount of rGO increases from 5 to 8 %.

Although CdS is the most studied sulfur containing photocatalyst for H_2 generation, the toxicity of Cd^{2+} makes convenient to find alternatives that can be environmentally more benign. Besides seeking for other transition metal to replace Cd^{2+}, the combination of metal sulfides having narrow band gap with wide band gap metal oxides, the former acting as light harvesters for the wide bandgap oxide, is known to increase the stability of the photocatalyst, while still enjoying high photocatalytic performance. In one of the examples combining metal oxides, sulfides and graphene, a photoelectrode constituted by TiO_2 nanorods on transparent

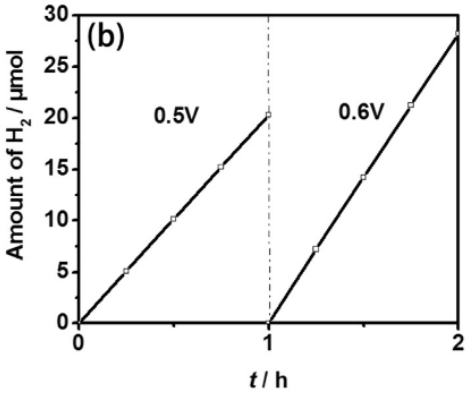

Figure 13. Temporal evolution of H_2 upon visible light illumination of $Zn_{0.5}Cd_{0.5}S$/rGO composite film photoanode at two different bias potentials immersed in an aqueous solution containing Na_2S (0.1 M) and Na_2SO_3 (0.1 M) in the working electrode chamber and NaOH (0.1 M) in the counter electrode chamber. Reprinted with permission from ref.[103]. Copyright (2014) ScienceDirect.

FTO electrode was modified by consecutive deposition cycles in which Bi_2S_3 and rGO were deposited[104]. The resulting composite is schematically represented in Figure 14, where the proposed role of each of the components has been indicated. The Bi_2S_3 and rGO containing material was denoted as "smart umbrella" sensitized TiO_2 nanorods. It was found that this photoelectrode has an optimal bias potential of 0.4 V *vs* NHE to maximize the photocurrent efficiency, whose maximum value was 1.2 ± 0.02 %. It was assumed that the photocurrent was related with the ability of the system to promote water splitting although no evidence for H_2 evolution was provided. Concerning photostability of the composite, also in the present case the common electrolyte solution used in metal sulfides consisting in a mixture of Na_2S and Na_2SO_3 was employed. It has been already commented that it is likely that the presence of S^{2-} ions contributes decisively to the apparent photostability of the metal sulfide.

In another work, Jia and co-workers deposited electrochemically $MoSe_2$ by reduction of Na_2MoO_4 and H_2SeO_3 in a NaAcO/HAcO aqueous buffered solution on an electrode containing rGO mixed with polyimide (PI)[105]. SEM images of the resulting photoelectrode indicate the presence of $MoSe_2$ NPs with a particle concentration that depends on the electrodeposition time.

Photoelectrochemical measurements of $MoSe_2$/rGO/PI photoelectrode indicate that $MoSe_2$ behaves as p-type semiconductor. The system enjoys an excellent reversibility and stability. This $MoSe_2$/rGO/PI electrode exhibits electrocatalytic and photoelectrocatalytic activity for H_2

evolution, the performance improving when the amount of $MoSe_2$ deposited increases, achieving a maximum current

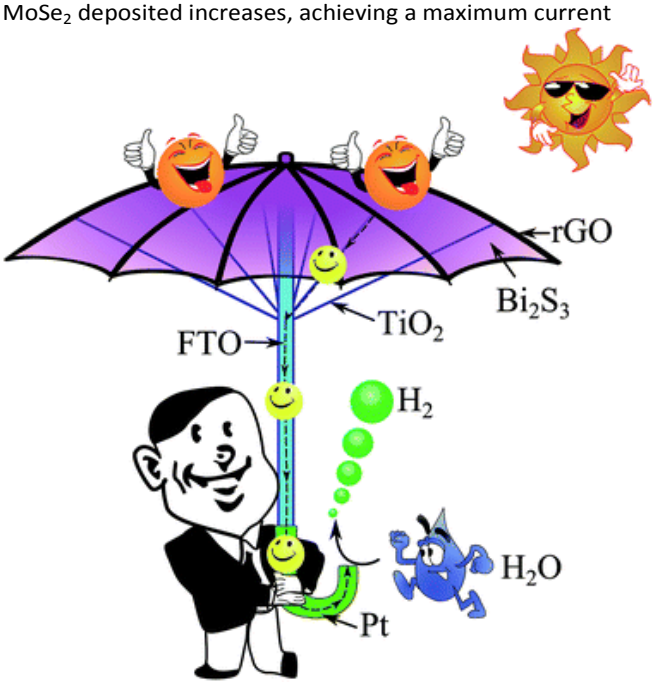

Figure 14. Schematic diagram of the "smart-umbrella" Bi_2S_3/rGO-modified TiO_2 nanorods structure. The Bi_2S_3 NPs act as the "canopy" and can efficiently harvest sunlight. The rGO sheet layers and 1D TiO_2 NRs act as the "ribs" and "stretchers", respectively, and can quickly transport electrons. The FTO conductive layer acts as the "shaft". The Pt counter electrode serves as the "handle". Reproduced from ref.[104] with permission from The Royal Society of Chemistry.

density of 29 mA·cm^{-2} at -0.8 V *vs* SCE in the dark. This cathodic current increases upon illumination. The most remarkable feature was the diminution of the free energy barrier of discharge for H_2 generation, due to the small size of $MoSe_2$ NPs and high surface area to rGO composite. A value of 82 mV·dec^{-1} suitable for practical application of hydrogen evolution reaction catalysts was obtained from the Tafel plot for $MoSe_2$ /rGO/PI.

A three component structure ITO/rGO/CdS/Ag_2S electrode having nanometric thickness has been reported by Wang and co-workers with enhanced photoelectrochemical efficiency for hydrogen generation than related ITO/CdS electrode[63]. The purpose of the multilayer assembled was to extend the photoresponse of the CdS by including a narrow band gap metal sulfide (Ag_2S) and increase charge separation, electron mobility and conductivity by the presence of rGO.

The structured three-component ITO/rGO/CdS/Ag_2S electrode was prepared stepwise by depositing consecutively each component. Initially, GO coating transparent ITO was electrochemically reduced to rGO at an optimal voltage of -0.75 V *vs* Ag/AgCl. Subsequently, the layer of CdS was fabricated by the so-called successive ionic layer adsorption and reaction (SILAR) in which ITO/rGO electrode was immersed for 20 s in two different aqueous solutions containing Cd^{2+} and S^{2-}, respectively, rinsing the electrode with distilled water after each step. Deposition of CdS was performed for 10, 20 and 30 cycles, found an optimal performance for the electrode prepared in 20 cycles. Analogously Ag^+ was deposited following also a similar method for a number of cycles (10, 20 and 30). It was again found that also 20 cycles result in the optimal performance of the electrode. Other configurations in which the order of the CdS and Ag_2S layers was inverted (ITO/rGO/CdS/Ag_2S *vs* ITO/rGO/Ag_2S/CdS) were also found less efficient, presumably due to the misalignment of the energy levels of CdS and Ag_2S. SEM images of ITO/rGO/CdS/Ag_2S at different stages of electrode preparation show the morphology of each layer, i.e., the 2D morphology to rGO, the spherical shape of NPs of 25-50

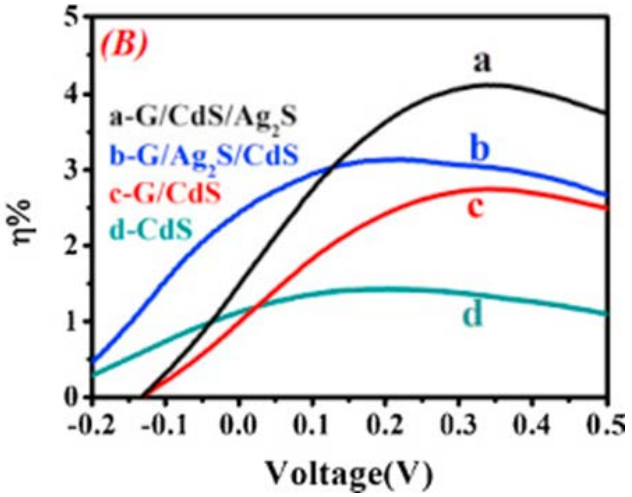

Figure 15. Efficiency for hydrogen generation of (a) ITO/rGO/CdS/Ag_2S, (b) ITO/rGO/Ag_2S/CdS, (c) ITO/rGO/CdS and (d) ITO/CdS. Reprinted with permission from ref. [63]. Copyright (2014) ScienceDirect.

nm for CdS and the nanorod shape of 30-60 nm diameter and 100-200 nm length for Ag_2S, respectively. The thickness of the optimal performing electrode was 40 nm for rGO, 30 nm for the CdS layer and 40 nm for the Ag_2S film. Interestingly, although it is claimed that Ag_2S nanorods grow perpendicular to the ITO electrode and the lengths of these nanorods according to TEM images is between 100-110 nm the thickness of the Ag_2S layer was of 40 nm. The thickness of Ag_2S rGO (about 40 nm) appears to be much smaller than the length of the nanorods. Comparing with control materials in the absence of rGO, it is suggested that the presence of rGO is beneficial to accelerate the nucleation growth of the CdS particles, since in the absence of rGO much less uniform layers are observed.

As commented above the purpose of the preparation of combined CdS and Ag_2S layers is to expand the visible light absorption of the composite electrode towards the near infrared region due to the narrow band gap (0.92 eV) of Ag_2S as compared to CdS (2.43 eV), while still preserving the ability to generate hydrogen. These assumptions were confirmed by comparing the photoelectrochemical activity of ITO/rGO/CdS that was smaller (3.45 mA·cm^{-2}) than the three components ITO/rGO/CdS/Ag_2S (5.18 mA·cm^{-2}). Figure 15 shows the plot of the hydrogen generation efficiencies for a serie of CdS photoelectrodes showing the advantage of the multicomponent assembly.

The maximum hydrogen generation efficiency upon illumination in UV-Vis range achieved was 4.11 % with a

maximum generation rate of 221 µmol·h^{-1} at photocurrent density of 5.18 mA·cm^{-2} at 0.55 V *vs* Ag/AgCl. It is proposed that this high efficiency rises from the large percentage of e^-/h^+ separation and the increased charge mobility due to the appropriate energy level alignment of the sulfides (Figure 16). Specifically by polarization of the electrode, the energy levels of Ag_2S increase and, then, after absorption of one long wavelength photon, conduction band electron of Ag_2S can move to the conduction band of CdS and then on rGO, decreasing in this way the recombination rate. In summary, the superior performance of ITO/rGO/CdS/Ag_2S is proposed to arise from the light harvesting ability of Ag_2S and the subsequent electron migration from Ag_2S to CdS and rGO. It is should be, however, commented that as previously indicated for other CdS photoelectrodes, the main drawback of sulfides is the need of Na_2S as electrolyte to stabilize CdS avoiding its conversion to the corresponding oxides.

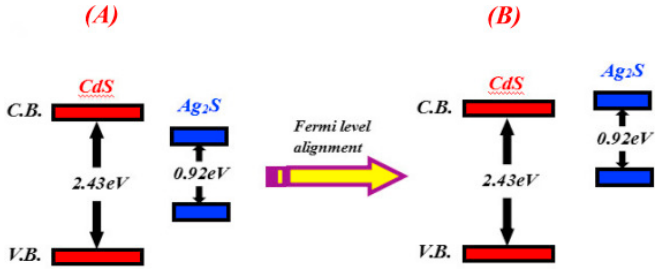

Figure 16. Relative energy levels of CdS, Ag2S (A) before and (B) after Fermi level alignment. Reprinted with permission from ref. [63]. Copyright (2014) ScienceDirect.

Table 2 summarizes those graphene based photoelectrodes for water splitting commented in this section as well as their working conditions and H_2 evolution.

Table2. Summary of the graphene containing photoelectrodes for H_2 evolution with indication of the applied bias potential and sacrificial agent.

Sample	Bias(V)	Sacrificial	H_2 evolution	Ref.
$BiVO_4$-rGO	0.8	0.1M Na_2SO_4	0.75 µmol/h	92
TiO_2/rGO/Cu_2O	0.6	CH_3OH	631.6 µmol/h·m^2	94
$Cd_xZn_{1-x}S$/rGO	0.6	Na_2S/Na_2SO_3	12.05 µmol/h·cm^2	100
TiO_2 /Bi_2S_3/rGO	0.4	Na_2S/Na_2SO_3	1.2 %[a]	102
$MoSe_2$/rGO/PI	-0.6	H_2SO_4	82 mV/dec[b]	66
rGO/CdS/Ag_2S	0.55	Na_2S/Na_2SO_3	221 µmol/h	62

[a] referred to photocurrent efficiency. [b] Obtained from Tafel plot.

Photoelectrochemical pollutant degradation and organic molecules.

Besides hydrogen generation, PEC can also be efficient for degradation of pollutants in aqueous solutions. Dyes are convenient probes to evaluate the activity of photoelectrodes for pollutant degradation, since the process can be followed by optical absorption spectroscopy. In one of these works dealing with dye decolorization, it has been found that rGO deposited on ordered TiO_2 nanotubes (TNT) arrays increases the efficiency of TNT arrays as photoelectrode for the degradation of methyl orange under visible light irradiation[106]. TNT arrays were fabricated by anodization of metallic Ti foil[107, 108]. Then, rGO was deposited by dipping TNT in an aqueous suspension of GO, submitting the resulting electrode to hydrothermal heating in an autoclave at 180 °C for 4 h to perform reduction of GO. Although rGO coated TNT arrays were not calcined, but XRD shows that the material contains some anatase phase, but probably in lesser extent than if the TNTs would have been calcined. SEM image indicates that rGO coats the top surface and it is also penetrates partially inside the TNT holes. The presence of rGO produces an apparent shift of the absorption band onset of about 20 nm, appearing for rGO-TNT composite about 418 nm (Figure 17). rGO-TNT electrodes exhibit an enhanced photocurrent of about 8.4 times higher than that of TNT electrodes. EIS suggests that the photocurrent enhancement observed for rGO-TNT is apparently due to the faster electron transport and the highest charge separation efficiency of photogenerated e^-/h^+ pairs in TNT. These positive effects have been attributed to the presence of rGO, since the arc of the impedance spectrum is smaller for rGO-TNT systems than for TNT electrodes. This photocurrent enhancement due to the presence of rGO is accompanied by a remarkable efficiency for methyl orange degradation of about 5 times higher than that of TNT (Figure 18). It was claimed that this higher photoelectrochemical efficiency is due to a combination of effects, including the shift of 20 nm of the onset of the absorption band, the increase of

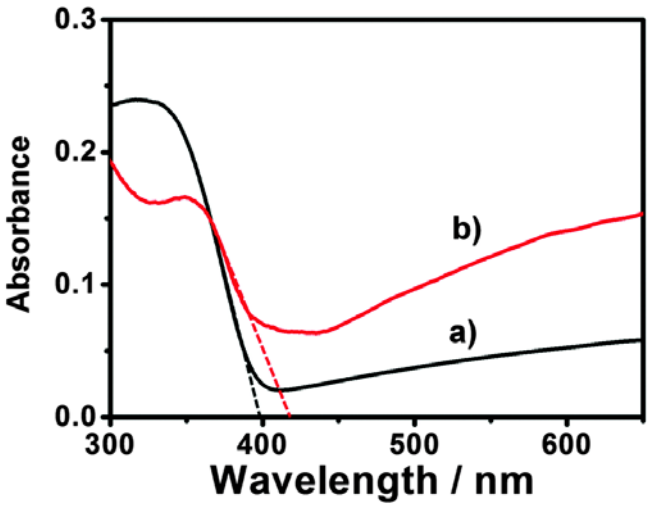

Figure 17. Diffuse reflectance UV-Vis absorption spectra of as-prepared (a) TNT and (b) rGO-TNT nanostructures. Reproduced from ref. [106] with permission from The Royal Society of Chemistry.

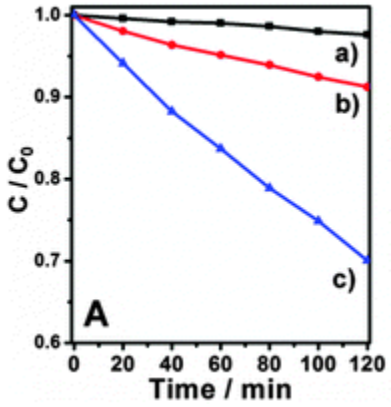

Figure 18. Photoelectrocatalytic activity for the degradation of methyl orange solution under visible-light irradiation (a) no catalyst, (b) TNT and (c) rGO-TNT electrodes. Reproduced from ref. [106] with permission from The Royal Society of Chemistry.

the surface area, the beneficial increase of the charge separation efficiency and the higher e^- mobility introduced by the presence of graphene.

Besides dyes, other organic molecules can also be decomposed by PEC. Thus, Ye and co-workers reported a photoanode consisting in Pt NPs supported on TiO_2 and rGO was prepared by simultaneous Pt (VI) and GO reduction with methanol in the presence of TiO_2 (P25)[109]. The Pt loading was about 20 % that is a very large percentage considering similar Pt-containing samples used in photocatalysis in where Pt loading is about 1 %. The presence of TiO_2 in the system has several benefits as the increase in the electrochemical surface area (96.7 $m^2 \cdot g^{-1}$) compared to Pt/G (46.5 $m^2 \cdot g^{-1}$) or commercially available of Pt on carbon (48.9 $m^2 \cdot g^{-1}$). TiO_2 also promotes the electrooxidation of methanol by Pt and, importantly, also increases the photocurrent upon UV irradiation by a factor of 2.5 with respect to commercial Pt/Si, meaning that there is an increase of methanol oxidation. This increase was due to the combination of electro- and photocatalysis, because of the presence of Pt and TiO_2 in $Pt/TiO_2/G$ composite. The role of G in the photoelectrocatalytic reaction was proposed to be as acceptor of photogenerated e^- from TiO_2 that, then, are transferred from G to Pt, thus, increasing the efficiency of charge separation. $Pt/TiO_2/G$ has an important positive feature that is the lack of influence of the presence of CO as poison. It is known in Pt-containing electrodes that CO is a strong poison for methanol oxidation reaction. However, when TiO_2 and G are present, the surface hydroxyl groups on these two components cause the fast CO oxidation alleviating the CO poisoning effect on Pt NPs.

Chronoamperometry in methanol (1 M)/H_2SO_4 (1 M) shows that the stability of $Pt/TiO_2/G$ composite is higher than analogous Pt/G or commercial Pt/C, whose activity decays for methanol oxidation in a few seconds (Figure 19), due to the generation of CO as poison. When TiO_2 is present, photocatalytic oxidation of CO to CO_2 minimizes this poisoning mechanism, increasing considerably the photoelectrode activity and stability. Figure 18 provides a comparison of the temporal evolution of current density of various Pt containing electrodes for methanol oxidation under UV irradiation

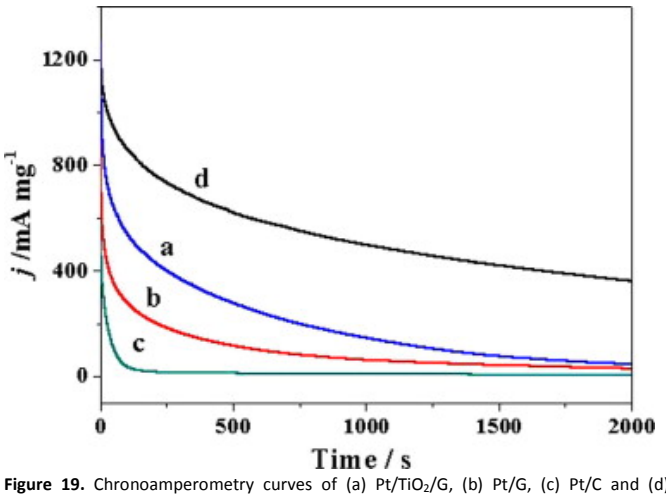

Figure 19. Chronoamperometry curves of (a) $Pt/TiO_2/G$, (b) Pt/G, (c) Pt/C and (d) Pt/TiO_2 under UV irradiation in the N_2 saturated solution of 1 M CH_3OH + 0.5 M H_2SO_4 at 0.67 V for 2000 s. Reprinted with permission from ref. [109]. Copyright (2014) ScienceDirect.

showing the better performance of $Pt/TiO_2/G$.

Table 3 summarizes those graphene-based photoelectrodes for organics degradation discussed in this section as well as their working conditions and performance.

Table3. Summary of the graphene-based photoelectrodes for pollutant degradation with indication of the applied bias potential, pollutant or organic molecule mineralized and the corresponding performance.

Sample	Bias(V)	Pollulant	Performance	Ref.
rGO-TNT	1.0	Methyl orange	$3 \cdot 10^{-3}$ min^{-1}	104
$Pt/TiO_2/G$	100 mV/s [b]	CH_3OH oxidation	1349 mA/mg [a]	107

[a] referred to forward peak current density under 20 min UV irradiation and. [b] CV curves scan rate.

Conclusions

The present review has shown that, similarly to what has been reported in photocatalysis, also in PEC the presence of graphene increases to photoelectrode efficiency with respects to analogous materials without this component. The reasons for this beneficial effect of the presence of graphene seem to be the electrical conductivity together with a higher electrochemical surface area, a higher efficiency of e^-/h^+ charge separation and a higher e^- mobility from the semiconductor to the electrode. It can be concluded that the positive influence of the presence of graphene in the photoelectrode appears to be general for all the reported studies related to CO_2 reduction, H_2 generation and for decomposition of organic molecules and pollutants (Figure 20) ant it is likely to be general for any other photoelectrocatalytic process.

Nevertheless, the use of graphene-based materials in photoelectrodes for solar fuel production and environmental remediation presents still some limitations that must be overcome. In spite of the theoretical large surface area that has been reported for graphene, it has been found that in operating conditions not all the graphene surface is accessible for the electrolyte, reducing ion diffusion and limiting Faradaic

efficiency. Probably structuring of graphene in a 3D sponge of micrometric dimensions will be a way to combine the advantages of graphene and the increase in electrochemical area, favouring electrolyte contact. Moreover, the typical graphene based material employed in PEC is rGO is known to contain defects and impurities in the form of vacancies or oxygenated functional groups, among others. The control of these defects can serve to find adequate balance between conductivity in the photoelectrodes and hydrophilicity/hydrophobicity to interact with substrates. Therefore, the rational design of these defects should be taken into consideration in order to enhance the photoelectrocatalytic activity of these materials minimizing negative impacts in electrode conductivity.

The general goal in this area should be to show the stability of the photoelectrodes in long term (at least days and weeks, but hopefully years) operation, showing that they can reach efficiencies and product formation rates closer to commercial application for some of these considering the current interest processes.

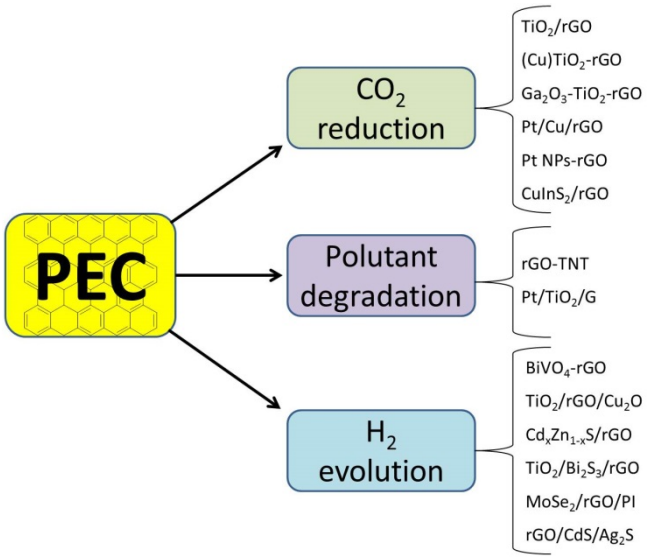

Figure 20. Summary of the application of the graphene-based photoelectrodes discussed in the review.

Acknowledgements

Financial support by the Spanish Ministry of Economy and Competitiveness (Severo Ochoa, CTQ2017-69153-CO2-R1 and Grapas) and Generalitat Valenciana (Prometeo 2013/014) is gratefully acknowledged. J.A. thanks the Universitat Politecnica de Valencia for a research associate contract.

Notes and references

1. Y. Tachibana, L. Vayssieres and J. R. Durrant, *Nat Photon*, 2012, **6**, 511-518.
2. S. Styring, *Faraday Discussions*, 2012, **155**, 357-376.
3. L. Hammarström and S. Hammes-Schiffer, *Accounts of Chemical Research*, 2009, **42**, 1859-1860.
4. T. P. Yoon, M. A. Ischay and J. Du, *Nat Chem*, 2010, **2**, 527-532.
5. D. Gust, T. A. Moore and A. L. Moore, *Accounts of Chemical Research*, 2009, **42**, 1890-1898.
6. K. Wenderich and G. Mul, *Chemical Reviews*, 2016, **116**, 14587-14619.
7. W.-J. Ong, L.-L. Tan, Y. H. Ng, S.-T. Yong and S.-P. Chai, *Chemical Reviews*, 2016, **116**, 7159-7329.
8. Y. Chen, X. Xin, N. Zhang and Y.-J. Xu, *Particle & Particle Systems Characterization*, 2017, DOI: 10.1002/ppsc.201600357.
9. S. Hu, *The Chemical Record*, 2016, **16**, 219-230.
10. J. L. White, M. F. Baruch, J. E. Pander, Y. Hu, I. C. Fortmeyer, J. E. Park, T. Zhang, K. Liao, J. Gu, Y. Yan, T. W. Shaw, E. Abelev and A. B. Bocarsly, *Chemical Reviews*, 2015, **115**, 12888-12935.
11. W.-J. Ong, L.-L. Tan, S.-P. Chai, S.-T. Yong and A. R. Mohamed, *ChemSusChem*, 2014, **7**, 690-719.
12. L.-j. Guo, Y.-j. Wang and T. He, *The Chemical Record*, 2016, **16**, 1918-1933.
13. X. Yang, R. Liu, Y. He, J. Thorne, Z. Zheng and D. Wang, *Nano Research*, 2015, **8**, 56-81.
14. E. S. Andreiadis, M. Chavarot-Kerlidou, M. Fontecave and V. Artero, *Photochemistry and Photobiology*, 2011, **87**, 946-964.
15. D. Pile, *Nat Photon*, 2012, **6**, 637-637.
16. V. Augugliaro, G. Camera-Roda, V. Loddo, G. Palmisano, L. Palmisano, J. Soria and S. Yurdakal, *The Journal of Physical Chemistry Letters*, 2015, **6**, 1968-1981.
17. X. Li, J. Yu, S. Wageh, A. A. Al-Ghamdi and J. Xie, *Small*, 2016, **12**, 6640-6696.
18. N. Zhang, Y. Zhang and Y.-J. Xu, *Nanoscale*, 2012, **4**, 5792-5813.
19. J. Liu, Y. Niu, X. He, J. Qi and X. Li, *Journal of Nanomaterials*, 2016, **2016**, 5.
20. A. Fujishima and K. Honda, *Nature (London)*, 1972, **238**.
21. D. Chen, H. Zhang, Y. Liu and J. Li, *Energy & Environmental Science*, 2013, **6**, 1362-1387.
22. T. Kasuga, M. Hiramatsu, A. Hoson, T. Sekino and K. Niihara, *Langmuir*, 1998, **14**, 3160-3163.
23. S. Rani, S. C. Roy, M. Paulose, O. K. Varghese, G. K. Mor, S. Kim, S. Yoriya, T. J. LaTempa and C. A. Grimes, *Physical Chemistry Chemical Physics*, 2010, **12**, 2780-2800.
24. A. Kudo, *International Journal of Hydrogen Energy*, 2006, **31**, 197-202.
25. X. Zong, H. Yan, G. Wu, G. Ma, F. Wen, L. Wang and C. Li, *Journal of the American Chemical Society*, 2008, **130**, 7176-7177.
26. P. V. Kamat, *The Journal of Physical Chemistry B*, 2002, **106**, 7729-7744.
27. P. Roy, S. Berger and P. Schmuki, *Angewandte Chemie International Edition*, 2011, **50**, 2904-2939.
28. K. S. Novoselov, A. K. Geim, S. V. Morozov, D. Jiang, Y. Zhang, S. V. Dubonos, I. V. Grigorieva and A. A. Firsov, *Science*, 2004, **306**, 666.
29. K. S. Novoselov, D. Jiang, F. Schedin, T. J. Booth, V. V. Khotkevich, S. V. Morozov and A. K. Geim, *Proceedings of the National Academy of Sciences of the United States of America*, 2005, **102**, 10451-10453.
30. Y. Noh, Y. Kim, S. Lee, E. J. Lim, J. G. Kim, S. M. Choi, M. H. Seo and W. B. Kim, *Nanoscale*, 2015, **7**, 9438-9442.

31. E. J. Lim, Y. Kim, S. M. Choi, S. Lee, Y. Noh and W. B. Kim, *Journal of Materials Chemistry A*, 2015, **3**, 5491-5500.
32. Y. Qu, Y. Gao, L. Wang, J. Rao and G. Yin, *Chemistry – A European Journal*, 2016, **22**, 193-198.
33. D. Higgins, M. A. Hoque, M. H. Seo, R. Wang, F. Hassan, J.-Y. Choi, M. Pritzker, A. Yu, J. Zhang and Z. Chen, *Advanced Functional Materials*, 2014, **24**, 4325-4336.
34. Y. Kim, Y. Noh, E. J. Lim, S. Lee, S. M. Choi and W. B. Kim, *Journal of Materials Chemistry A*, 2014, **2**, 6976-6986.
35. J. Yang, D. Voiry, S. J. Ahn, D. Kang, A. Y. Kim, M. Chhowalla and H. S. Shin, *Angewandte Chemie International Edition*, 2013, **52**, 13751-13754.
36. A. H. Castro Neto, F. Guinea, N. M. R. Peres, K. S. Novoselov and A. K. Geim, *Reviews of Modern Physics*, 2009, **81**, 109-162.
37. V. Singh, D. Joung, L. Zhai, S. Das, S. I. Khondaker and S. Seal, *Progress in Materials Science*, 2011, **56**, 1178-1271.
38. Y. Zhu, S. Murali, W. Cai, X. Li, J. W. Suk, J. R. Potts and R. S. Ruoff, *Advanced Materials*, 2010, **22**, 3906-3924.
39. Y. Liu, X. Dong and P. Chen, *Chemical Society Reviews*, 2012, **41**, 2283-2307.
40. Q. He, S. Wu, Z. Yin and H. Zhang, *Chemical Science*, 2012, **3**, 1764-1772.
41. S. Wu, Q. He, C. Tan, Y. Wang and H. Zhang, *Small*, 2013, **9**, 1160-1172.
42. Y. Shao, J. Wang, H. Wu, J. Liu, I. A. Aksay and Y. Lin, *Electroanalysis*, 2010, **22**, 1027-1036.
43. X. Huang, X. Qi, F. Boey and H. Zhang, *Chemical Society Reviews*, 2012, **41**, 666-686.
44. C. Xu, B. Xu, Y. Gu, Z. Xiong, J. Sun and X. S. Zhao, *Energy & Environmental Science*, 2013, **6**, 1388-1414.
45. S. Bose, T. Kuila, A. K. Mishra, R. Rajasekar, N. H. Kim and J. H. Lee, *Journal of Materials Chemistry*, 2012, **22**, 767-784.
46. K. Ellmer, *Nat Photon*, 2012, **6**, 809-817.
47. D. S. Hecht, L. Hu and G. Irvin, *Advanced Materials*, 2011, **23**, 1482-1513.
48. J. K. Wassei and R. B. Kaner, *Materials Today*, 2010, **13**, 52-59.
49. Y. Lee and J.-H. Ahn, *Nano*, 2013, **08**, 1330001.
50. F. Schwierz, *Nat Nano*, 2010, **5**, 487-496.
51. P. Avouris, Z. Chen and V. Perebeinos, *Nat Nano*, 2007, **2**, 605-615.
52. P. Avouris, *Nano Letters*, 2010, **10**, 4285-4294.
53. C. Huang, C. Li and G. Shi, *Energy & Environmental Science*, 2012, **5**, 8848-8868.
54. L. K. Putri, L.-L. Tan, W.-J. Ong, W. S. Chang and S.-P. Chai, *Applied Materials Today*, 2016, **4**, 9-16.
55. L. K. Putri, W.-J. Ong, W. S. Chang and S.-P. Chai, *Applied Surface Science*, 2015, **358, Part A**, 2-14.
56. X. Li, J. Yu, S. Wageh, Al, A. A. Ghamdi and J. Xie, *Small*, 2016, **12**, 6640-6696.
57. Z. Zhang, T. Zheng, X. Li, J. Xu and H. Zeng, *Particle & Particle Systems Characterization*, 2016, **33**, 457-472.
58. C. Tang, H.-F. Wang, X.-L. Zhu, B.-Q. Li and Q. Zhang, *Particle & Particle Systems Characterization*, 2016, **33**, 473-486.
59. J. Yu, J. Jin, B. Cheng and M. Jaroniec, *Journal of Materials Chemistry A*, 2014, **2**, 3407-3416.
60. W.-J. Ong, L.-L. Tan, S.-P. Chai and S.-T. Yong, *Chemical Communications*, 2015, **51**, 858-861.
61. Q. Xiang, B. Cheng and J. Yu, *Angewandte Chemie International Edition*, 2015, **54**, 11350-11366.
62. A. Adán-Más and D. Wei, *Nanomaterials*, 2013, **3**.
63. B. Wang, Z. Liu, J. Han, T. Hong, J. Zhang, Y. Li and T. Cui, *Electrochimica Acta*, 2015, **176**, 334-343.
64. X. Chen and S. S. Mao, *Chemical Reviews*, 2007, **107**, 2891-2959.
65. X. Chen, S. Shen, L. Guo and S. S. Mao, *Chemical Reviews*, 2010, **110**, 6503-6570.
66. J. Low, B. Cheng, J. Yu and M. Jaroniec, *Energy Storage Materials*, 2016, **3**, 24-35.
67. M.-Q. Yang and Y.-J. Xu, *Nanoscale Horizons*, 2016, **1**, 185-200.
68. J. Zhang, Q. Xu, Z. Feng, M. Li and C. Li, *Angewandte Chemie International Edition*, 2008, **47**, 1766-1769.
69. G. R. Bamwenda, S. Tsubota, T. Nakamura and M. Haruta, *Journal of Photochemistry and Photobiology A: Chemistry*, 1995, **89**, 177-189.
70. A. Fujishima, T. N. Rao and D. A. Tryk, *Journal of Photochemistry and Photobiology C: Photochemistry Reviews*, 2000, **1**, 1-21.
71. S. N. Habisreutinger, L. Schmidt-Mende and J. K. Stolarczyk, *Angewandte Chemie International Edition*, 2013, **52**, 7372-7408.
72. G. R. Dey, *Journal of Natural Gas Chemistry*, 2007, **16**, 217-226.
73. J. Low, J. Yu and W. Ho, *The Journal of Physical Chemistry Letters*, 2015, **6**, 4244-4251.
74. W.-J. Ong, L.-L. Tan, S.-P. Chai, S.-T. Yong and A. R. Mohamed, *Nano Energy*, 2015, **13**, 757-770.
75. W.-J. Ong, L. K. Putri, Y.-C. Tan, L.-L. Tan, N. Li, Y. H. Ng, X. Wen and S.-P. Chai, *Nano Research*, 2017, **10**, 1673-1696.
76. M. R. Hasan, S. B. A. Hamid and W. J. Basirun, *Applied Surface Science*, 2015, **339**, 22-27.
77. M. R. Hasan, S. B. Abd Hamid, W. J. Basirun, S. H. Meriam Suhaimy and A. N. Che Mat, *RSC Advances*, 2015, **5**, 77803-77813.
78. J. M. T. A. Fischer, M. Hankel and D. J. Searles, *The Journal of Physical Chemistry C*, 2015, **119**, 29044-29051.
79. M. R. Hasan, S. B. Abd Hamid, W. J. Basirun, Z. Z. Chowdhury, A. E. Kandjani and S. K. Bhargava, *New Journal of Chemistry*, 2015, **39**, 369-376.
80. J. Cheng, M. Zhang, J. Liu, J. Zhou and K. Cen, *Journal of Materials Chemistry A*, 2015, **3**, 12947-12957.
81. J. Cheng, M. Zhang, G. Wu, X. Wang, J. Zhou and K. Cen, *Environmental Science & Technology*, 2014, **48**, 7076-7084.
82. O. K. Varghese, M. Paulose, T. J. LaTempa and C. A. Grimes, *Nano Letters*, 2009, **9**, 731-737.
83. J. Cheng, M. Zhang, G. Wu, X. Wang, J. Zhou and K. Cen, *Solar Energy Materials and Solar Cells*, 2015, **132**, 606-614.
84. M. Gratzel, *Nature*, 2001, **414**, 338-344.
85. Y. Xu and M. A. A. Schoonen, *American Mineralogist*, 2000, **85**, 543.
86. J. Yuan, P. Wang, C. Hao and G. Yu, *Electrochimica Acta*, 2016, **193**, 1-6.
87. K. Maeda and K. Domen, *The Journal of Physical Chemistry Letters*, 2010, **1**, 2655-2661.
88. Y. Lu, B. Ma, Y. Yang, E. Huang, Z. Ge, T. Zhang, S. Zhang, L. Li, N. Guan, Y. Ma and Y. Chen, *Nano Research*, 2017, **10**, 1662-1672.

89. L. K. Putri, B.-J. Ng, W.-J. Ong, H. W. Lee, W. S. Chang and S.-P. Chai, *ACS Applied Materials & Interfaces*, 2017, **9**, 4558-4569.
90. Q. Wang, T. Hisatomi, Q. Jia, H. Tokudome, M. Zhong, C. Wang, Z. Pan, T. Takata, M. Nakabayashi, N. Shibata, Y. Li, I. D. Sharp, A. Kudo, T. Yamada and K. Domen, *Nat Mater*, 2016, **15**, 611-615.
91. C. Acar, I. Dincer and G. F. Naterer, *International Journal of Energy Research*, 2016, **40**, 1449-1473.
92. P. K. Dubey, P. Tripathi, R. S. Tiwari, A. S. K. Sinha and O. N. Srivastava, *International Journal of Hydrogen Energy*, 2014, **39**, 16282-16292.
93. J. Luo, D. Li, Y. Yang, H. Liu, J. Chen and H. Wang, *Journal of Alloys and Compounds*, 2016, **661**, 380-388.
94. Y. H. Ng, A. Iwase, A. Kudo and R. Amal, *The Journal of Physical Chemistry Letters*, 2010, **1**, 2607-2612.
95. K. Chun-Ren, G. Jyun-Sheng, S. Yen-Hsun and T. Jyh-Ming, *Nanotechnology*, 2016, **27**, 435405.
96. W. Fan, X. Yu, H.-C. Lu, H. Bai, C. Zhang and W. Shi, *Applied Catalysis B: Environmental*, 2016, **181**, 7-15.
97. U. Sim, T.-Y. Yang, J. Moon, J. An, J. Hwang, J.-H. Seo, J. Lee, K. Y. Kim, J. Lee, S. Han, B. H. Hong and K. T. Nam, *Energy & Environmental Science*, 2013, **6**, 3658-3664.
98. F. Carraro, L. Calvillo, M. Cattelan, M. Favaro, M. Righetto, S. Nappini, I. Píš, V. Celorrio, D. J. Fermín, A. Martucci, S. Agnoli and G. Granozzi, *ACS Applied Materials & Interfaces*, 2015, **7**, 25685-25692.
99. E. W. Keong Koh, C. H. Chiu, Y. K. Lim, Y.-W. Zhang and H. Pan, *International Journal of Hydrogen Energy*, 2012, **37**, 14323-14328.
100. Y. Li, H. Wang, L. Xie, Y. Liang, G. Hong and H. Dai, *Journal of the American Chemical Society*, 2011, **133**, 7296-7299.
101. H. Li, K. Yu, C. Li, Z. Tang, B. Guo, X. Lei, H. Fu and Z. Zhu, 2015, **5**, 18730.
102. Y. Yu, J. Zhang, X. Wu, W. Zhao and B. Zhang, *Angewandte Chemie International Edition*, 2012, **51**, 897-900.
103. J. Zhang, W. Zhao, Y. Xu, H. Xu and B. Zhang, *International Journal of Hydrogen Energy*, 2014, **39**, 702-710.
104. X. Wang, J. Xie and C. M. Li, *Journal of Materials Chemistry A*, 2015, **3**, 1235-1242.
105. L. Jia, X. Sun, Y. Jiang, S. Yu and C. Wang, *Advanced Functional Materials*, 2015, **25**, 1814-1820.
106. C. Zhai, M. Zhu, Y. Lu, F. Ren, C. Wang, Y. Du and P. Yang, *Physical Chemistry Chemical Physics*, 2014, **16**, 14800-14807.
107. G. Dai, J. Yu and G. Liu, *The Journal of Physical Chemistry C*, 2011, **115**, 7339-7346.
108. H. E. Prakasam, K. Shankar, M. Paulose, O. K. Varghese and C. A. Grimes, *The Journal of Physical Chemistry C*, 2007, **111**, 7235-7241.
109. L. Ye, Z. Li, L. Zhang, F. Lei and S. Lin, *Journal of Colloid and Interface Science*, 2014, **433**, 156-162.